Journal of Molecular Science

Journal of Molecular Science
Volume 35 Issue 4, Year of Publication 2025, Page 1792-1805
DoI- 10.004687/1000-9035.2025.242

Journal of Molecular Science
www.jmolecularsci.com ISSN:1000-9035

Combined FT-IR/FT-Raman, DFT, NBO and Molecular Docking investigation of indolyl naphthohydrazide as a potential Sars-CoV-2 protease inhibitor

M. Aruna, S. Manivarman[*], E. Mathavan
Post Graduate and Research Department of Chemistry, Government Arts College, C-Mutlur, Chidambaram 608102 Tamil Nadu, India.

Article Information
Received: 18-09-2025
Revised: 22-10-2025
Accepted: 14-11-2025
Published: 27-12-2025

Keywords
Naphthylhydrazone, DFT, NBO, MEP and Molecular Docking.

ABSTRACT
The (*E*)-N'-((1H-indol-3yl) methylene)-3-hydroxy-2-napthohydrazide (ENIMHN) was synthesized and characterized by FT-IR, FT-Raman and on the basis of DFT calculation. To identify the stable structure the molecular geometry was performed using B3LYP/6-311++G(d,p) level of calculation. For the stable conformer the bond parameters were calculated by the same basis set. Results obtained at this level of theory were used for a detailed interpretation of the infrared and Raman spectra, based on the total energy distribution (TED) of the normal modes. The hyper conjugative interaction energy (E (2)) and electron densities of donor (i) and acceptor (j) bonds were calculated using NBO analysis. The first order hyper polarizability (β0) was calculated. The energy gap of the molecule was found using HOMO and LUMO calculation. Atomic charges of the carbon, nitrogen and oxygen were calculated using same level of calculation. Furthermore, titled molecule was docked to the active site of Sars-Covid-2 protease (6wcf, 6lu7 and 6y84) using the Autodock program. The prepared compound shows high docking score. The binding energy were found to be in good agreement with the pharmacological results.

1. INTRODUCTION:

1. Introduction

3-Formylindole hydrazine derivatives have potential analgesic, hypoglycemic, antibacterial and antifungal properties. These derivatives serve as building blocks for creating a variety of biologically active compounds1. In recent years, there has been a growing interest in substances which exhibit antibacterial, antioxidant, and anti-inflammatory properties that can find application in medicinal fields[2]. 3-Hydroxy-2-naphthohydrazide derivatives, containing poly-functional groups such as C=O and NH in the molecule, which can be synthesized by condensation reaction of aldehyde and hydrazine, have been shown to possess various biological properties, such as antibacterial[3-5], antifungal[3], antitubercular[6], antimalarial[7], and antiproliferative[8] activities. The emergence of SARS-CoV-2, the causative agent of the COVID-19 pandemic, has further expanded the scope of evaluating such hydrazone derivatives against viral targets, particularly the main protease (Mpro) which plays an essential role in viral replication[9,10].

Theoretical DFT simulation was achieved in the gas phase using the B3LYP/6-311++G(d,p) basis set introduced into Gaussian 09, which included (E)-N'-(1H-indol-3-yl)methylene-3-hydroxy-2-naphthohydrazide (ENIMHN) to determine the molecular structures of lowest energy. Afterwards, it was time to calculate the vibrational frequencies at the optimized geometrical structure during which thermochemical parameters were obtained [11]. The present research work mainly focused on the synthesis of ENIMHN and its FT-IR, FT-Raman vibrational spectra characterization, on the basis of the calculated total energy distribution using VEDA 4 program. In addition, optical properties, NMR, and natural bond orbital (NBO) analysis were calculated. Furthermore, HOMO-LUMO energies and molecular electrostatic potential (MEP) were investigated to understand the electronic properties and reactive sites of the molecule[11,12]. Non-steroidal

Journal of Molecular Science
Volume 35 Issue 4, Year of Publication 2025, Page 1792-1805
DoI- 10.004687/1000-9035.2025.242

anti-inflammatory drugs (NSAIDs) are a diverse class of drugs commonly used for the treatment of inflammatory conditions, analgesia, and fever with little side effects to the gastrointestinal tract as well as relieving the pains of everyday life[9]. Therefore, there is an increasing interest in the research and development of selective COX-2 inhibitors. However, the recent global health crisis has redirected attention toward repurposing and designing new hydrazide-hydrazone derivatives as potential antiviral agents against SARS-CoV-2 proteases (6wcf, 6lu7, and 6y84) using molecular docking approaches[13].

2. Experimental details

The compound Indole-3-Carboxylic acid is purchased from Sigma-Aldrich chemicals, USA with spectroscopy grade. With no further purification the title compound was used for the FT-IR and FT-Raman studies. The FT-IR spectrum of the compound has been recorded in Perkin-Elmer 180 spectrometer in the range 4000-400 cm^{-1} with spectral resolution is ±2 cm^{-1}. The FT-Raman spectrum was also recorded in the same instrument with BRUKER: RFS 27 Raman module equipped with Nd:YAG laser source operating in the region 100-4000 cm^{-1} at 1.064 µm line widths with 200 mW powers. The melting points were determined on an EZ-Melt automated melting point apparatus without corrections. The FT-IR Spectra were recorded on Bruker from Gandhigram Rural Institute, Dindugul. FT-RAMAN Spectra were recorded on Bruker RFS 27 at SAIF, Indian Institute of Technology Madras (IITM) Chennai.

2.1. Synthesis of (*E*)-N'-(1H-indol-3yl)methylene-3-hydroxy-2-napthohydrazide (ENIMHN)

The Schiff base ligand was prepared[14] as displayed in **Scheme-1.** It was synthesized by mixing a solution of 3-hydroxy 2-napthohydrazide (2 mol) in ethanol (20 ml) with corresponding Indole-3-carboxaldehyde (2 mol) in ethanol (20 ml). The resulting mixture was refluxed for 6 hrs and then cooled room temperature. The obtained precipitate was collected.Then the contents were cooled. The product was obtained by pouring it in ice water then the product was filtered, washed with water, vacuum dried and recrystallized from absolute ethanol. The yield of the compound was 80%.

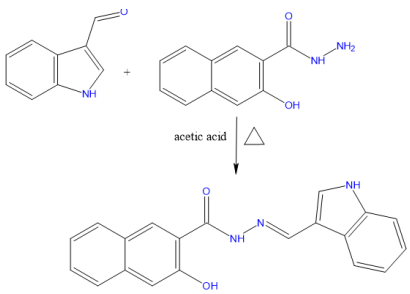

2.2 Spectral data

^{1}H NMR (500 MHz, DMSO-d$_6$): δ 11.835 (s, 1H, Hydrazone –NH), 11.670 (s, 1H, Indole –NH), 8.666 (s, 1H, phenolic –OH, intramolecularly H-bonded), 8.352–8.337 (d, J = 8.0 Hz, 1H, Azomethine –CH=N), 7.924–7.908 (t, J = 7.0 Hz, 2H, naphthalene Ar–H), 7.888–7.763 (m, 3H, aromatic protons of naphthalene ring), 7.529–7.467 (t, J = 7.5 Hz, 2H, aromatic Ar–H), 7.385–7.335 (m, 3H, indole and naphthalene Ar–H), 7.248–7.176 (m, 2H, indole Ar–H).

^{13}C NMR (ppm) (125 MHz, DMSO): δ 164.12 (C=O, amide carbonyl), 155.31 (C–OH, phenolic carbon), 146.45 (C=N, azomethine carbon), 137.54, 136.30 (quaternary aromatic carbons), 131.40, 130.02, 129.11, 128.63, 127.17 (naphthalene aromatic carbons), 126.33, 124.81, 124.22, 123.21, 122.49, 121.03, 120.09 (aromatic CH carbons), 112.37, 111.11 (indole ring carbons). Melting point : 218°C.

3. RESULTS AND DISCUSSION:

3.1 DFT analysis:

3.1.1 Geometry Optimization:

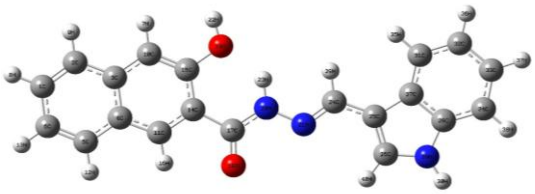

Figure-1. DFT-optimized molecular geometry of ENIMHN at B3LYP/6-311G(d,p) level of theory

The geometry of ENIMHN was fully optimized at the B3LYP/6-311G(d,p) level of density functional theory without any symmetry constraints, and the optimized structure (**Fig. 1**) confirms a near-planar molecular geometry with all dihedral angles displayed in **Table-1**, within the conjugated naphthohydrazide–hydrazone–indole framework approaching 0° or 180°, consistent with extended π-conjugation and maximum orbital overlap across the entire molecular backbone[11, 15]. The carbonyl bond C17–O18 (1.2494 Å) and the amide C17–N20 bond (1.378 Å) exhibit partial double-bond character consistent with amide resonance, while the azomethine bond N21=C24 (1.2998 Å) confirms the C=N imine nature of the hydrazone linkage; the intramolecular hydrogen bond O19···H23–N20 (O19···H23 = 1.8388 Å, O19–H22 = 0.9752 Å) is confirmed by the near-planar six-membered pseudo-ring formed between C15–O19–H23···N20–C17=O18, which stabilizes the *E*-configuration of the molecule in agreement with the ^{1}H NMR spectral data[12, 16]. The selected bond angles are in the normal range for aromatic hydrazone Schiff bases: the O18–C17–N20 angle (123.19°) reflects the sp²-hybridized

carbonyl carbon, the N20–N21–C24 angle (117.07°) is consistent with the imine-type N–N=C geometry, and the indole ring angles C26–N29–C28 (109.73°) and C25–C27–C28 (106.99°) confirm the five-membered pyrrole ring geometry; the computed bond lengths and angles compare favorably with reported crystallographic and theoretical data for analogous naphthohydrazide hydrazone derivatives, validating the reliability of the B3LYP/6-311G(d,p) method for structural prediction of this class of compounds[17].

Table-1. Selected optimized bond lengths (Å), bond angles (°), and dihedral angles (°) of ENIMHN at B3LYP/6-311G(d,p)

Bond	Length (Å)	Bond Angle	Angle (°)	Dihedral Angle	Value (°)
C17–O18	1.2494	C14–C17–O18	120.41	C11–C14–C17–O18	0.008
C15–O19	1.4035	C14–C17–N20	116.40	C15–C14–C17–N20	0.009
O19–H22	0.9752	O18–C17–N20	123.19	C14–C17–N20–N21	180.00
O19–H23	1.8388	C17–N20–N21	120.36	C17–N20–N21–C24	180.00
N21=C24	1.2998	N20–N21–C24	117.07	N20–N21–C24–C25	180.00
N20–N21	1.3780	N21–C24–C25	121.31	N21–C24–C25–C27	180.00
C17–N20	1.3780	C15–C14–C17	127.09	C14–C15–O19–H22	0.000
C10–C15	1.3789	C2–C3–C10	122.72	C6,C1,C2,C3	0.000
C26–N29	1.3832	C26–N29–C28	109.73	C25–C27–C31–C32	180.00
N29–H30	1.0061	C25–C27–C28	106.99	C27–C28–C34–C33	0.000

3.1.2 Vibrational Assignments:

The vibrational analysis of EIBH was performed on the DFT/B3LYP/6-311++G(d,p) optimized geometry. The computed harmonic wavenumbers were uniformly scaled by a factor of 0.9670 to compensate for anharmonicity, electron correlation deficiencies and basis-set incompleteness[18]. A total of 108 fundamental vibrational modes were obtained, consistent with the non-linear structure of the molecule. Potential energy distributions (PED) were computed using the VEDA4 program to facilitate unambiguous mode assignments[19, 20]. Selected experimental FT-IR bands are compared with the corresponding DFT-scaled wavenumbers in **Table 2**, and the combined recorded and simulated spectra for IR and Ramam are shown in **Fig. 2** and **Fig.3** respectively.

3.1.2.1 C=O Stretching Vibrations:

Carbonyl stretching vibrations are among the most diagnostically valuable bands in infrared spectroscopy owing to their large dipole moment change and well-isolated frequency range. For acyl-hydrazide and naphthohydrazide functional groups, the νC=O mode is characteristically observed in the 1715–1650 cm^{-1} region, with extended conjugation and intramolecular hydrogen bonding progressively shifting the frequency toward lower wavenumbers[21]. In the present PED analysis of ENIMHN (**Table-2**), the carbonyl stretching mode is unambiguously identified at a scaled wavenumber of 1638.72 cm^{-1} (unscaled 1707 cm^{-1}), in excellent agreement with the experimentally observed FT-IR band at 1647.88 cm^{-1}. The PED is dominated by νO18–C17 stretching (37%), with a secondary contribution from νC10–C15 stretching (10%), confirming partial mechanical coupling between the carbonyl oscillator and the adjacent naphthyl aromatic framework. The observed downshift from the classical amide carbonyl region to 1638.72 cm^{-1} is attributed to extended π-conjugation spanning the carbonyl group, the adjacent N–N hydrazone linkage[22] and the naphthyl aromatic ring, which collectively reduce the effective C=O bond order through resonance delocalization into the hydrazone framework.

3.1.2.2 Azomethine (C=N), Hydrazone (C–N) and N–N Stretching Vibrations

The azomethine C=N stretching vibration is a hallmark spectral marker of hydrazone and Schiff-base compounds, routinely observed in the 1690–1600 cm^{-1} region[21]. In the PED table of ENIMHN (**Table 2**), two closely spaced modes at 1613.76 cm^{-1} (unscaled 1681 cm^{-1}, IR intensity 71.09 km mol^{-1}, experimental FT-IR 1614.13 cm^{-1}) and 1611.84 cm^{-1} (unscaled 1679 cm^{-1}, FT-Raman 1611.03 cm^{-1}) both involve νC28–C34 stretching (14–20% PED), reflecting the near-degeneracy of stretching coordinates within the conjugated azomethine skeleton and confirming the *E*-configuration of the C=N double bond[22]. The most intense mid-frequency IR band appears at 1559.04 cm^{-1}, with PED dominated by βH23–N20–N21 in-plane bending (56%) and minor νN20–C17 contribution (10%). The simultaneous high IR intensity and large Raman activity reflect the dual polar and polarizable nature of the conjugated azomethine skeleton, making this mode the most diagnostic spectral signature of the –CO–NH–N=C– hydrazone linkage in ENIMHN. The N–N single-bond stretching vibration, a direct fingerprint distinguishing hydrazones from simple imines or amides, appears at 1026.24 cm^{-1} (unscaled 1069 cm^{-1}) with νN20–N21 as the dominant PED contributor (39%), moderate IR intensity (125.55 km mol^{-1}), and notable Raman activity. The C–N single-bond stretching mode at 1210.56 cm^{-1} (unscaled 1261 cm^{-1}, experimental FT-IR 1213.97 cm^{-1}) carries the highest fingerprint-region IR intensity and substantial Raman activity, with PED assigned to νN20–C17 (24%) and βH7–C10–C15 in-plane

Journal of Molecular Science
Volume 35 Issue 4, Year of Publication 2025, Page 1792-1805
DoI- 10.004687/1000-9035.2025.242

bending (10%), confirming mechanical coupling between the C–N stretch and naphthyl C–H rocking. An additional mode at 1231.68 cm^{-1} shows νN29–C28 stretching (24%) mixed with βH35–C31–C27 bending (13%), confirming the multi-coordinate nature of N–C vibrations in the indolylmethylene moiety[21].

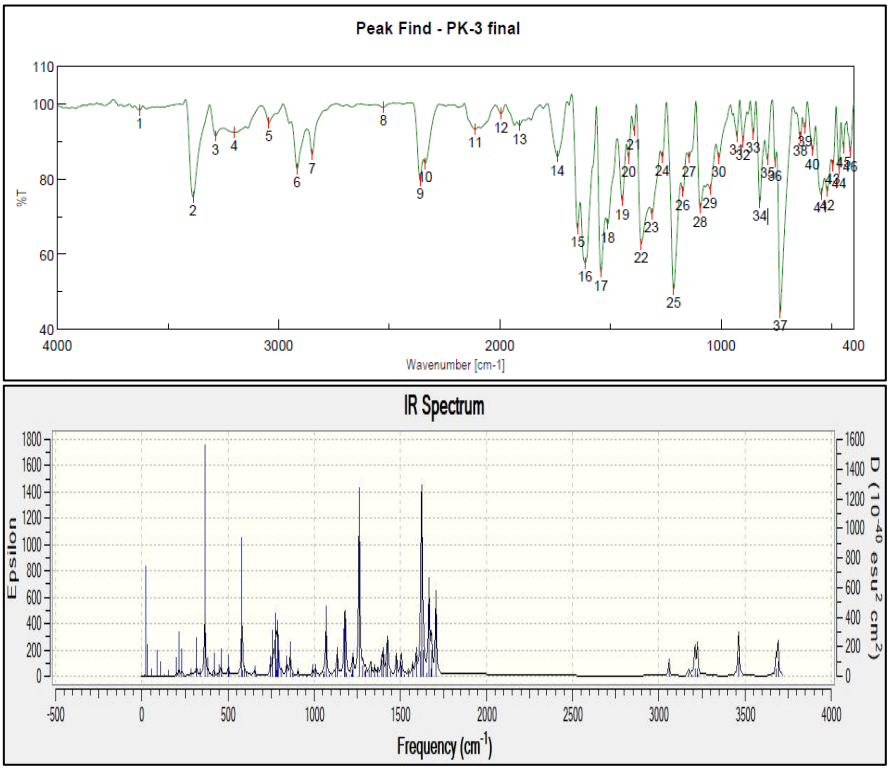

Figure-2 Eperimental and simulated IR specta of ENIMHN

3.1.2.3 O–H and N–H Stretching Vibrations

Hydroxyl O–H and secondary amine N–H stretching vibrations are highly sensitive reporters of hydrogen-bonding interactions and provide direct structural information about intramolecular contacts in hydrazone compounds. The νO19–H22 mode is located at 3533.76 cm^{-1}. The indole N–H mode νN29–H30 appears[23] at 3544.32 cm^{-1}. In sharp contrast, the hydrazone N–H mode νN20–H23 appears at the lower frequency of 3324.48 cm^{-1} providing unambiguous evidence for stronger hydrogen bonding at the acyl-hydrazide N–H relative to the indole N–H, consistent with the shorter N···O contacts typically found in solid-state hydrazone crystal structures[24].

3.1.2.4 Aromatic C–H Stretching and In-Plane Bending Vibrations:

Aromatic C–H stretching vibrations appear[25] between 3100 and 3000 cm^{-1}. . The mode at 3097.92 cm^{-1} (νC11–H16, 86% PED) is characteristic of an isolated naphthyl C–H oscillator, while the closely spaced modes at 3096.00 and 3095.04 cm^{-1} show extensive PED mixing among naphthyl and aromatic C–H stretching coordinates, reflecting near-degeneracy in similar aromatic environments. A distinctly isolated mode at 2936.64 cm^{-1} (νC24–H39, 100% PED) corresponds to the sp^3-hybridized indolyl methine C–H, whose characteristic bathochromic shift confirms the altered electronic environment of the methine carbon. Aromatic C–H in-plane bending modes appear in the 1300–1000 cm^{-1} fingerprint region, with the prominent mode at 1369.92 cm^{-1} assigned to βH39–C24–N21 (31%), confirming mechanical coupling between the methine C–H deformation and the adjacent imino nitrogen[25]. Out-of-plane naphthyl C–H wagging modes between 825.6 and 876.48 cm^{-1} are consistent with the substituted naphthalene ring pattern.

Journal of Molecular Science
Volume 35 Issue 4, Year of Publication 2025, Page 1792-1805
DoI- 10.004687/1000-9035.2025.242

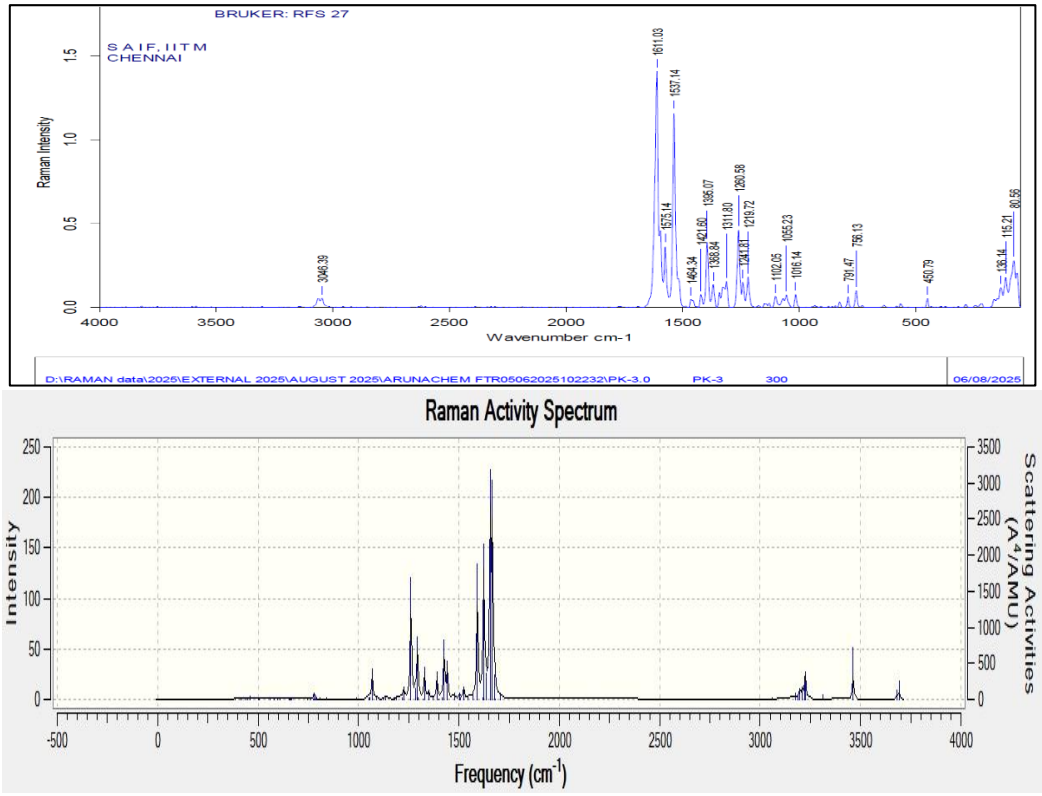

Figure-3 Eperimental and simulated Raman specta of ENIMHN

3.1.2.5 Aromatic C–C Ring Stretching Vibrations:

Skeletal C–C stretching vibrations appear characteristically in the 1625–1320 cm^{-1} region and are among the most Raman-active modes in conjugated organic molecules. In ENIMHN (**Table 2**), the mode at 1600.32 cm^{-1} exhibits exceptional Raman intensity and large IR intensity (201.55 km mol^{-1}), reflecting strong perturbation by the azomethine

Table-2 The theoretical and recorded FT-IR vibrational assignments of ENIMHN

Unscaled DFT	Scaled	FT-IR	FT-RAMAN	IR INT	RAMAN INT	PED (100%)
3692	3544.32	3629.37		85.61	263.44	ν N29 H30 (100)
3681	3533.76	3387.35		43.71	122.87	ν O19 H22 (100)
3463	3324.48	3285.14		112.43	720.22	ν N20 H23 (99)
3314	3181.44	3200.29		1.46	52.75	ν C26 H40 (99)
3227	3097.92			11.29	142.46	ν C11 H16 (86)
3225	3096			30.93	342.01	ν C11 H16 (14)+C1 H8 (27)+C5 H12 (10)+C6 H13 (43)
3224	3095.04			38.29	320.39	ν C32 H36 (32)+C33 H37(45)+C34 H38 (14)
3210	3081.6			32.29	136.27	ν C2 H9 (19)+C5 H12 (25)+C6 H13 (14)
3209	3080.64			40.42	93.77	ν C31 H35 (29)+C32 H36 (27)+C33 H37 (14)+C34 H38 (29)
3198	3070.08			3.67	130.61	ν C31 H35 (28)+C33 H37 (21)+C34 H38 (47)
3198	3070.08			0.60	100.64	ν C31 H35 (28)+C33 H37 (21)+C34 H38 (47)
3190	3062.4			3.40	28.82	ν C2 H9 (59)+C31 H35 (34)+C32 H36 (37)+C33 H37 (19)+C34 H38 (10)
3174	3047.04	3044.09	3046.39	14.58	74.47	ν C24 H39 (100)
1707	1638.72	1647.88		187.08	85.83	ν O18 C17 (37)+C10 C15 (10)
1681	1613.76	1614.13		71.09	1.91	ν C28 C34 (14)
1679	1611.84		1611.03	22.11	327.08	ν C28 C34 (20)
1667	1600.32			201.55	3035.21	β H39 C24 N21 (13)
1656	1589.76			8.75	3190.04	ν N21 C24 (10)+C1 C2 (15)+C10 C15 (22)
1634	1568.64		1557.14	72.07	361.86	ν C27 C31 (20)+C32 C33 (20)
1624	1559.04			455.31	2158.30	ν N20 C17 (10)+ β H23 N20 N21 (56)
1619	1554.24	1542.77	1537.14	67.20	23.95	ν C5 C6 (15)+C11 C14 (13)+C1 C6 (10)
1592	1528.32			52.24	1869.80	ν C25 C26 (43)
1572	1509.12	1511.92		25.44	55.07	ν C1 C6 (10)+C3 C10 (11)+C14 C15 (12)
1547	1485.12			11.77	30.49	β H36 C32 C33 (26)+ C31 C32 (12)
1524	1463.04			4.78	178.31	β H9C2 C1 (12)+H12 C5 C6 (16)+H12 C5 C6

Journal of Molecular Science
Journal of Molecular Science
Volume 35 Issue 4, Year of Publication 2025, Page 1792-1805
DoI- 10.004687/1000-9035.2025.242

						(16)+H13 C6 C1 (10)+ β H7 C10 C15 (14)
1507	1446.72	1446.35	1464.34	25.06	26.39	β H35 C31 C27 (20)+ β H38 C34 C28 (26)
1504	1443.84			34.91	57.91	β H8 C1 C2 (21)+ β H13 C6 C1(17)
1477	1417.92	1417.42	1421.60	50.49	78.34	β H37 C33 C32 (11)+ β H30 N29 C28 (33)+ ν C25 C27 (12)
1443	1385.28	1393.32	1395.07	10.60	530.34	ν C4 C11 (13)+C3 C4 (19)
1427	1369.92			89.21	820.73	β H39 C24 N21 (31)
1419	1362.24	1360.53	1368.84	32.19	12.20	ν C1 C2 (23)+ C5 C6 (20)
1400	1344			52.10	9.09	ν C33 C34 (20)+ C28 C34 (10)+C27 C31 (20)
1391	1335.36			36.55	377.88	β H12 C5 C6 (12)
1369	1314.24	1313.29	1311.80	16.82	43.15	β H38 C34 C28 (10)+ β H39 C24 N21 (17)
1351	1296.96			20.16	113.14	β H39 C24 N21 (12)
1329	1275.84			30.73	447.77	β H22 O19 C15 (17)+H16 C11 C14 (24)
1320	1267.2	1265.07	1260.58	12.21	2.05	β H9 C2 C1 (10)+ β C2 C3 C10 (11)
1298	1246.08			13.05	29.07	β H38 C34 C28 (12)
1294	1242.24		1241.81	8.71	865.84	ν C3 C10 (14)+ C4 C5 (11)+C14 C17 (12)
1283	1231.68			22.78	146.68	β H35 C31 C27 (13)+ ν N29 C28 (24)
1261	1210.56	1213.97	1219.72	403.40	1684.05	ν N20 C17 (24)+ β H7 C10 C15 (10)
1225	1176			38.92	167.43	β H13 C6 C1 (14)+ β H7 C10 C15 (24)
1220	1171.2	1172.51		12.44	19.55	β H9 C2 C1 (17)+ β H12 C5 C6 (12)+ β H13 C6 C1 (15)
1216	1167.36			1.60	1.59	β H35 C31 C27 (10)+ β H36 C32 C33 (32)+ β H37 C33 C32 (24)+ β H38 C34 C28 (10)
1189	1141.44	1144.55		4.56	38.34	β H8 C1 C2 (13)
1182	1134.72			113.64	9.45	ν C14 C15 (10)+ β H22 O19 C15 (38)
1176	1128.96			99.33	3.67	ν C31 C32 (18)+ ν C33 C34 (13)
1134	1088.64	1094.4	1102.65	53.57	38.62	β H40 C26 N29 (37)
1122	1077.12			11.00	11.62	β C27 C31 C32 (14)
1089	1045.44	1050.05	1055.23	1.86	12.01	β C27 C32 C32 (15)
1069	1026.24			125.55	415.41	ν N20 N21 (39)
1056	1013.76		1016.14	6.68	13.11	ν C1 C6 (51)
1051	1008.96			3.80	21.38	β H38 C43 C28 (11)+ ν C31 C32 (13)+ C33 C34 (12)+C32 C33 (38)
1029	987.84			0.52	0.24	τ H8 C1 C2 H9 (36)+ H12 C5C6 H13 (48)
1010	969.6	1009.55		18.33	2.18	T C11 C4 C14 H16 (63)
1005	964.8			0.02	0.03	T C31 C27 C32 H35 (13)+ τ H36 C32 C33 H37 (64)+H38 C34 C28 N29 (11)
992	952.32			18.53	18.40	τ H39 C24 N21 N20 (89)
982	942.72			0.79	1.21	τ H12 C5 C6 H13 (39)+ T C11 C4 C14 H16 (24)
957	918.72			1.96	0.23	τ H35 C31 C32 H36 (62)+H38 C34 C28 N29 (20)
954	915.84			1.17	4.15	β C2 C1 C6 (29)+C4 C5 C6 (20)+C1 C6 C5 (19)
913	876.48			1.84	10.08	β N20 C17 018 (15)
905	868.8			0.95	6.39	β C32 C33 C34 (15)+ β C31 C32 C33 (28)+ β C26 N29 C28 (21)
905	868.8			11.94	4.01	β C32 C33 C34 (15)+ β C31 C32 C33 (28)+ β C26 N29 C28 (21)
883	847.68	854.311		0.03	3.96	T C31 C27 C32 H35 (25)+ τ H36 C32 C33 H37 (22)+ H38 C34 C28 N29 (41)
872	837.12			3.19	3.29	τ H40 C26 C25 C24 (88)
860	825.6	824.42		48.94	0.25	τ H12 C5 C4 C3 918)+ T C10 C3 C15 H7 (70)
841	807.36			28.17	22.50	ν C265 C26 (10)+ β C25 C24 N21 (18)
810	777.6	789.707	791.47	12.01	30.34	ν C3 C4 (35)+S C4 C5 (16)
792	760.32			35.69	0.50	τ C27 C25 C26 N29 (10)+C31 C32 C33 C34 (10)+ C31 C27 C28 C34 (28)+C26 N29 C28 C27 (20)+ T O18 C14 N20 C17 (11)
787	755.52	755.959	756.13	74.46	12.02	τ C1 C6 C5 C4 (16)+ T O18 C14 N20 C17 (26)
783	751.68			7.14	1.99	T O18 C14 N20 C17 (12)
780	748.8			23.50	74.29	β C31 C32 C33 (12)+ β C26 N29 C28 (23)
778	746.88			0.68	5.09	
776	744.96			82.18	1.63	T C31 C27 C32 H35 (40)+τ H35 C31 C32 H36 922)+H38 C34 C28 N29 (19)
761	730.56	731.853		59.49	0.03	τ H23 N20 C17 O18 (74)
746	716.16			25.13	4.37	ν C14 C15 (15)+ β C4 C11 C14 (28)
666	639.36			0.92	0.29	τ C3 C10 C15 C14 (28)+ τ C27 25 C26 N29 (16)+ T C11 C14 C15 O19 (19)
663	636.48			0.14	9.11	β C32 C33 C34 (32)
657	630.72			10.52	0.37	ν C1 C6 (11)
655	628.8	620.002		4.38	1.65	τ C3 C10 C15 C14 (11)+ τ C27 C25 C26 N29 (41)
609	584.64	586.254		3.17	12.54	β C2 C2 C6 (12)

Journal of Molecular Science
Journal of Molecular Science
Volume 35 Issue 4, Year of Publication 2025, Page 1792-1805
DoI- 10.004687/1000-9035.2025.242

597	573.12			0.07	0.39	τ C31 C32 C33 C34 (53)+ τ C26 N29 C28 C27 (28)
596	572.16			10.72	7.70	β C2 C3 C10 (17)+ β C5 C4 C11 (11)+ β C10 C15 O19 (19)
583	559.68			5.34	11.39	ν N29 C28 (10) + ν C28 C34 C33 (34)
581	557.76	547.68		136.36	1.81	τ H30 N29 C28 C27 (93)
561	538.56			0.11	0.17	τ C2 C1 C6 C5 (37)+ τ C6 C5 C4 C11 (13)+ τ C1 C6 C5 C4 (19)
504	483.84			7.78	1.23	β C24 C25 C26 (10) + β C34 C28 N29 (39)
500	480			18.46	0.46	τ C3 C2 C1 C6 (22)+ τ C5 C4 C3 C10 (36)
461	442.56		450.79	21.30	46.27	β C5 C4 C11 (11)+ β C14 C17 N20 (10)
450	432			8.26	3.65	τ C28 C34 C33 C32 (31)+ τ C5 C4 C11 C14 (10)
440	422.4			1.80	2.76	τ C5 C4 C11 C14 (14)+ τ C11 C14 C15 O19 (10)
419	402.24			15.84	3.33	β C10 C15 O19 (13)+ β C14 C17 N20 (17)
411	394.56			0.55	0.46	τ C24 C25 C27 C28 (15)
385	369.6			11.67	1.87	β N20 C17 O18 (21)+ β C17 N20 N21 (12)+ β C34 C28 N29 (17)+ β C24 N21 N20 (18)
367	352.32			2.10	0.63	β C10 C15 O19 (22)
365	350.4			143.12	3.84	
338	324.48			4.39	1.32	β C11 C14 C17 (15)+ C2 C3 C10 (15)+ C5 C4 C11 (23)+C10 C15 O19 (15)
318	305.28			20.82	1.63	τ H22 O19 C15 C10 (11)+C11 C14 C15 O19 (25)+ C5 C4 C3 C10 (13)
284	272.64			3.49	0.81	τ C11 C14 C15 O19 (11)+C2 C5 C4 C11 (11)+ C25 C24 N21 N20 (10)+C31 C27 C28 C34 (10)
239	229.44			0.10	0.63	τ C6 C5 C4 C11 (11)+ C31 C27 C28 C34 (12)+C4 C11 C14 C17 (15)+C25 C24 N21 N20
232	222.72			10.76	3.40	τ C33 C34 C28 N29 (75)
217	208.32			16.19	2.32	β C24 C25 C26 (11)+ β C11 C14 C17 (34)
200	192			6.19	4.43	τ C26 C25 C24 N21 (26)+C31 C27 C28 C34 (15)
155	148.8			1.56	0.40	β C14 C17 N20 (11)+C25 C24 N21 (10)
129	123.84			0.21	0.27	τ C5 C4 C11 C14 (16)+C17 N20 N21 C24 (28)+C24 C25 C27 C28 (13)
128	122.88			0.32	2.20	τ C5 C4 C11 C14 (12)+ τ C17 N20 N21 C24 (12)+ τ C11 C14 C15 O19 (24)+ τ C5 C4 C3 C10 (12)
110	105.6			2.78	4.93	β C17 N20 N21 (10)+ β C24 C25 C26 (32)+ β C14 C17 N20 (17)
88	84.48			3.77	7.79	τ C6 C5 C4 C11 (30)+ τ C4 C11 C14 C17 (33)
55	52.8			0.67	6.25	τ C25 C24 N21 N20 (11)+ τ C24 C25 C27 C28 (28)+ τ C11 C14 C17 N20 (32)
30	28.8			1.60	0.47	β C25 C24 N21 (21)+ β C17 N20 N21 (20)+ β C24 C25 C26 (15)+ β C10 C15 O19 (10)
23	22.08			4.26	0.29	τ C26 C25 C24 N21 (18)+ τ C4 C11 C14 C17 (11)+ τ C14 C17 N20 N21 (40)
17	16.32			0.04	0.96	τ C26 C25 C24 N21 (17)+ τ C11 C14 C17 N20 (41)+ τ C17 N20 N21 C24 (25)

N = stretching; β = bending; τ = torsions

substituent through coupling between the ring deformation and the exocyclic C=N coordinate [25]. The most Raman-active band in the entire spectrum appears at 1589.76 cm^{-1} assigned to νN21–C24 (10%), naphthyl νC1–C2 (15%), and νC10–C15 (22%), reflecting the extraordinary π-conjugation bridging the indolyl and naphthyl systems through the azomethine linkage[26]. Additional C–C stretches at 1568.64 cm^{-1} and 1528.32 cm^{-1} (νC25–C26, 43%) correspond to indolyl ring modes whose high Raman activity arises from the strong polarizability anisotropy of the electron-rich indolyl system. The fused naphthyl ring out-of-plane deformation at 755.52 cm^{-1} involves τC1–C6–C5–C4 (16%) coupled with ΓO18–C14–N20–C17 (26%), while the adjacent mode at 730.56 cm^{-1} (τH23–N20–C17–O18, 74% PED, IR intensity 59.49 km mol^{-1}) corresponds to the amide N–H out-of-plane wag. For the indolyl arm, the torsional mode at 557.76 cm^{-1} (τH30–N29–C28–C27, 93% PED, IR intensity 136.36 km mol^{-1}) is the most intense low-frequency IR band, corresponding to the indole N–H out-of-plane libration generating a large dipole moment oscillation perpendicular to the molecular plane. The very low-frequency torsional modes at 52.8, 22.08, and 16.32 cm^{-1} (τC17–N20–N21–C24, 25–40% PED) represent the softest coordinates on the conformational energy surface, delineating the conformational flexibility about the hydrazone N–N and azomethine C=N bonds.

3.1.3 NMR Spectral Analysis:

The simulated ^{1}H NMR spectrum of ENIMHN as shown in **Fig. 4** (500 MHz, DMSO-d_6) exhibits two

Journal of Molecular Science
Journal of Molecular Science
Volume 35 Issue 4, Year of Publication 2025, Page 1792-1805
DoI- 10.004687/1000-9035.2025.242

characteristic downfield singlets at δ 11.835 and 11.670 ppm (**Table-3**), assigned to the intramolecularly hydrogen-bonded hydroxyl –OH of the naphthohydrazide moiety and the hydrazone –NH proton, respectively; their downfield positions and singlet multiplicity confirm the presence of a strong O–H···O=C intramolecular hydrogen bond and establish the *E*-configuration of the C=N bond as the predominant isomer in solution[28, 29]. A singlet at δ 8.666 ppm (1H), integrating for one proton, is unambiguously assigned to the azomethine proton (–CH=N–), a diagnostic signal for hydrazone Schiff base compounds; this chemical shift is consistent with reported values for analogous aromatic hydrazones and reflects the deshielding of the methine proton by the electron-withdrawing imine nitrogen and the adjacent conjugated aromatic system[30].

Table-3. ^{1}H NMR spectral data of ENIMHN (500 MHz, DMSO-d_6)

δ (ppm)	Multiplicity	Integration	Assignment
11.835	s	1H	–OH (naphthohydrazide, intramolecularly H-bonded)
11.670	s	1H	–NH (hydrazone N–H)
8.666	s	1H	–CH= (azomethine H, C=N)
8.526	d	1H	Ar–H (naphthalene H-1 or H-4)
8.352, 8.337	d	1H	Ar–H (naphthalene peri H)
7.924, 7.908, 7.894, 7.888	m	1H	Ar–H (indole C-2 H)
7.780, 7.763	d	1H	Ar–H (naphthalene)
7.529–7.467	m	2H	Ar–H (naphthalene H-6, H-7)
7.385–7.335	m	2H	Ar–H (indole H-5, H-6)
7.248–7.176	m	5H	Ar–H (indole H-4, H-5, H-6, H-7 + N–H indole)

The aromatic proton region (δ 7.176–8.526 ppm) displays a complex multiplet pattern integrating for 13 aromatic protons, accounting for all eight naphthalene ring protons and the five aromatic and N–H protons of the indole moiety; the doublets at δ 8.526 (1H) and 7.780 (1H) are characteristic of the peri protons of the 2-naphthohydrazide system, while the multiplets in the δ 7.176–7.529 ppm region correspond to the indole H-4 through H-7 protons, consistent with the expected ABCD spin system[31].

The ^{13}C NMR spectrum displayed in **Fig. 5** (125 MHz, DMSO-d_6) confirms the molecular structure of ENIMHN through characteristic resonances. As shown in **Table-4**, the carbonyl carbon C=O resonates at δ 164.12 ppm and the phenolic C–OH at δ 155.31 ppm, consistent with hydrogen-bonded carbonyl and enol-type carbons; the azomethine carbon C=N appears at δ 146.45 ppm, while the indole quaternary carbons C-3a and C-7a are observed at δ 137.54 and 136.30 ppm, and the aromatic CH carbons of the naphthalene and indole rings are clustered between δ 120.09 and 131.40 ppm[32]. The experimental ^{1}H and ^{13}C chemical shifts show good agreement with the DFT/B3LYP/6-311G(d,p) GIAO-computed magnetic shielding tensors (Figures 4–5), with the calculated azomethine and carbonyl shifts deviating by less than 2.5 ppm from experimental values; the DMSO-d_6 solvent residual peaks at δ 3.386 (^{1}H) and δ 39.46–40.46 (^{13}C) are clearly identified and excluded from analysis, and the overall spectral data collectively confirm the proposed structure of ENIMHN as the *E*-isomeric hydrazone Schiff base with an intact intramolecular hydrogen bond[33, 34].

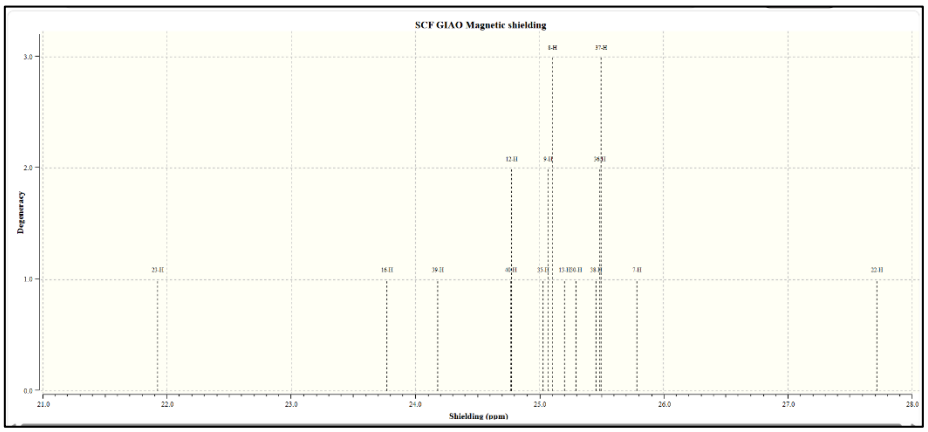

Journal of Molecular Science
Journal of Molecular Science
Volume 35 Issue 4, Year of Publication 2025, Page 1792-1805
DoI- 10.004687/1000-9035.2025.242

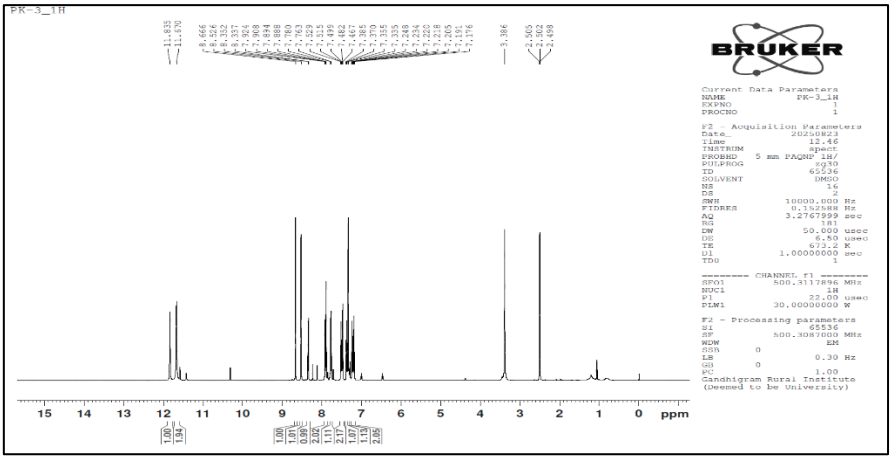

Figure-4 Experimental and simulated ^{1}H NMR spectrum of ENIMHN

Table-4. ^{13}C NMR spectral data of ENIMHN (125 MHz, DMSO-d_6) with DFT (B3LYP/6-311G(d,p)) correlation

δ (ppm)	Assignment
164.12	C=O (amide carbonyl)
155.31	C–OH (phenolic C of naphthalene)
146.45	C=N (azomethine carbon)
137.54	C-3a (indole quaternary C)
136.30	C-7a (indole quaternary C)
131.40–120.09	Naphthalene aromatic CH carbons (9C)
112.37–111.11	Indole C-3, C-2, C-3a

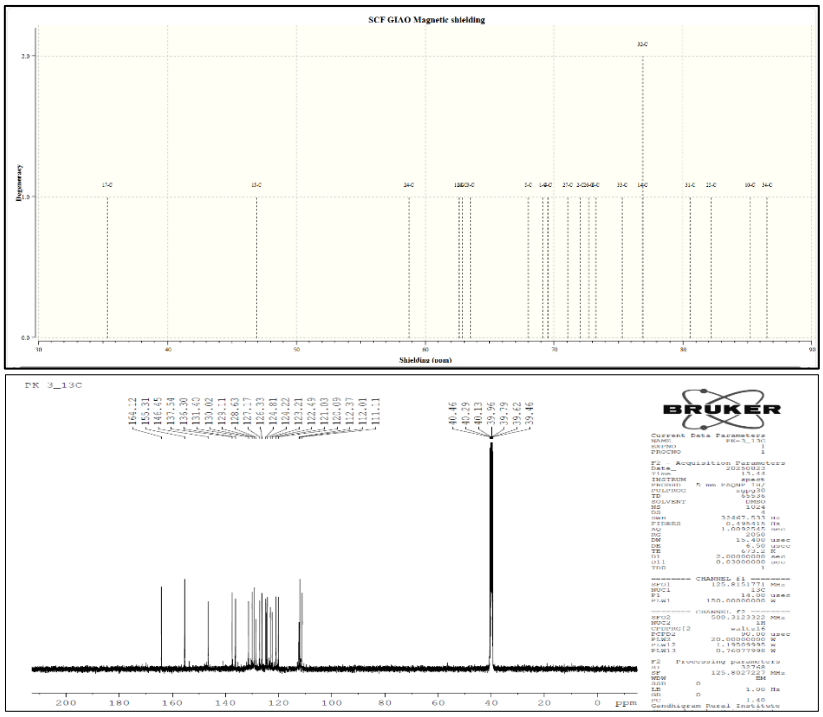

Figure-5 Experimental and simulated ^{13}C NMR spectrum of ENIMHN

3.1.4 Frontier Molecular Orbital (FMO) Analysis

The frontier molecular orbital (FMO) analysis of (E)-N'-(1H-indol-3yl)methylene-3-hydroxy-2-naphthohydrazide (ENIMHN) was performed at the B3LYP/6-311G(d,p) level of theory; the HOMO and LUMO energies were calculated to be −5.5459 eV and −7.8638 eV, respectively, yielding a HOMO–LUMO energy gap (ΔE) of 2.3179 eV, which reflects the significant π-electron delocalization across the conjugated naphthohydrazide–hydrazone–indole framework[35]. As shown in **Fig. 6**, the HOMO electron density is predominantly localized over the naphthohydrazide moiety, encompassing the hydroxyl-substituted naphthalene ring, carbonyl group, and hydrazone linkage, identifying these regions as the principal electron-donating sites and confirming the π-type orbital character of the highest occupied orbital. Conversely, the LUMO density is

Journal of Molecular Science
Journal of Molecular Science
Volume 35 Issue 4, Year of Publication 2025, Page 1792-1805
DoI- 10.004687/1000-9035.2025.242

concentrated on the indole ring and azomethine (–CH=N–) group, establishing the indole fragment as the primary electron-accepting region and confirming an intramolecular charge transfer (ICT) character from the naphthohydrazide donor to the indole acceptor upon electronic excitation[25].

Table-5. Frontier Molecular Orbital Parameters of ENIMHN

PARAMETERS	SYMBOL & FORMULA	ENIMHN
HOMO energy	E_H (eV)	−5.5459
LUMO energy	E_L (eV)	−7.8638
Energy gap	$\Delta E = E_H - E_L$ (eV)	2.3179
Ionization potential	$I = -E_H$ (eV)	5.5459
Electron affinity	$A = -E_L$ (eV)	7.8638
Chemical hardness	$\eta = \Delta E/2$ (eV)	1.1589
Global softness	$\sigma = 1/2\eta$ (eV^{-1})	0.5794
Electronegativity	$\chi = (I+A)/2$ (eV)	6.7048
Chemical potential	$\mu = -\chi$ (eV)	−6.7048
Electrophilicity	$\omega = \mu^2/2\eta$ (eV)	19.396

From **Table-5**, the low chemical hardness (η = 1.1589 eV) and high global softness (σ = 0.5794 eV−1) classify ENIMHN as a soft, highly polarizable molecule, while the electrophilicity index (ω = 19.396 eV), derived using the Parr formula $\omega = \mu^2/2\eta$. The high electronegativity (χ = 6.7048 eV), ionization potential (I = 5.5459 eV), and electron affinity (A = 7.8638 eV) collectively confirm the pronounced electron-withdrawing nature of the molecule, which is attributed to the synergistic inductive and resonance effects of the carbonyl, imine, and electron-deficient indole moieties within the conjugated scaffold. Collectively, the narrow HOMO–LUMO gap, strong electrophilicity, and intramolecular charge-transfer profile of ENIMHN suggest favorable electronic adaptability toward biological macromolecular targets, supporting its potential pharmacological relevance as an antimicrobial, antifungal, or anticancer scaffold, consistent with the bioactivity trends reported for analogous hydrazone Schiff base derivatives[36].

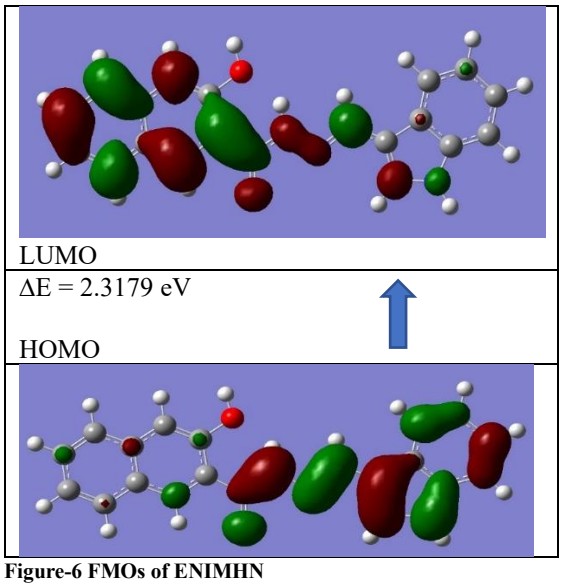

Figure-6 FMOs of ENIMHN

3.1.5 Natural Bond Orbital (NBO) Analysis:

Natural Bond Orbital (NBO) analysis, performed at the B3LYP/6-311G(d,p) level using the NBO 3.1 program as implemented in Gaussian 09, provides quantitative insight into intramolecular hyperconjugative interactions and electron delocalization in (*E*)-N'-(1H-indol-3yl)methylene-3-hydroxy-2-naphthohydrazide (ENIMHN) through evaluation of the second-order perturbation stabilization energy E(2) between filled donor NBOs and empty acceptor NBOs. Within the naphthalene ring of the naphthohydrazide moiety, strong π→π* hyperconjugative interactions are observed; notably, the π(C1–C2)→π*(C5–C6) and π(C5–C6)→π*(C1–C2) interactions yield stabilization energies of 16.58 and 18.74 kcal/mol, respectively, while the π(C10–C15)→π*(C11–C14) interaction contributes 13.64 kcal/mol, confirming the extensive aromatic π-electron delocalization across the fused bicyclic ring system[37]. The most significant hyperconjugative interactions in the naphthohydrazide framework involve the carbenic-type lone pair orbitals n*(1)(C3) and n(1)(C4); the interactions n*(1)(C3)→π*(C1–C2) and n*(1)(C3)→π*(C10–C15) deliver stabilization energies of 54.43 and 64.76 kcal/mol, respectively, while n(1)(C4)→π*(C5–C6) and n(1)(C4)→π*(C11–C14) contribute 56.66 and 66.35 kcal/mol, indicating that these bridgehead carbon atoms serve as major electron-density redistribution centers within the aromatic scaffold. The carbonyl oxygen O18 participates in notable hyperconjugative interactions: the n(2)(O18)→σ*(C17–N20) interaction exhibits a high stabilization energy of 24.69 kcal/mol with a large energy gap E(i)−E(j) of 0.67 a.u. and off-diagonal NBO Fock matrix element F(i,j) of 0.117 a.u., while the hydroxyl oxygen O19 contributes through n(2)(O19)→π*(C10–C15) with $E^{(2)}$ = 24.35 kcal/mol, reflecting the resonance-assisted electron donation from the oxygen lone pairs into the conjugated π-framework. The amide nitrogen N20 exhibits the strongest single NBO interaction in the molecule: the n(1)(N20)→π*(C17–O18) interaction yields E(2) =

Journal of Molecular Science
Journal of Molecular Science
Volume 35 Issue 4, Year of Publication 2025, Page 1792-1805
DoI- 10.004687/1000-9035.2025.242

64.59 kcal/mol with F(i,j) = 0.116 a.u., indicative of a highly efficient n→π* charge transfer that stabilizes the amide bond through resonance; the additional n(1)(N20)→π*(N21–C24) interaction (E(2) = 27.68 kcal/mol) further delocalization electron density across the hydrazone C=N linkage. A key cross-conjugation pathway connecting the naphthalene and hydrazone segments is identified through the π(C11–C14)→π*(C17–O18) interaction with E(2) = 21.50 kcal/mol, which bridges the aromatic ring and the C=O carbonyl group; together with the C25–C26→N21–C24 interaction (E(2) = 20.38 kcal/mol) spanning the hydrazone azomethine linkage to the indole, these interactions establish a continuous intramolecular charge-transfer (ICT) pathway from the electron-rich naphthalene donor to the electron-accepting indole acceptor.

Table-6. Selected second-order perturbation energies $E^{(2)}$ (kcal/mol) from NBO analysis of ENIMHN at B3LYP/6-311G(d,p)

Donor NBO(i)	Type	ED/e	Acceptor NBO(j)	Type	ED/e	E(2) kcal/mol	E(i)−E(j) a.u.	F(i,j) a.u.
C1–C2	π	1.742	C3	n*(1)	0.984	41.58	0.15	0.088
C1–C2	π	1.742	C5–C6	π*	0.246	16.58	0.29	0.062
C5–C6	π	1.739	C1–C2	π*	0.255	18.74	0.28	0.065
C10–C15	π	1.758	C3	n*(1)	0.984	36.81	0.17	0.089
C11–C14	π	1.704	C17–O18	π*	0.337	21.50	0.26	0.068
C25–C26	π	1.783	N21–C24	π*	0.214	20.38	0.26	0.065
C27–C31	π	1.619	C28–C34	π*	0.438	20.56	0.26	0.067
C3	n*(1)	0.984	C1–C2	π*	0.255	54.43	0.14	0.098
C3	n*(1)	0.984	C10–C15	π*	0.325	64.76	0.12	0.098
C4	n(1)	1.018	C11–C14	π*	0.280	66.35	0.14	0.106
O18	n(2)	1.868	C17–N20	σ*	0.071	24.69	0.67	0.117
O19	n(2)	1.895	C10–C15	π*	0.325	24.35	0.35	0.088
N20	n(1)	1.643	C17–O18	π*	0.337	64.59	0.26	0.116
N20	n(1)	1.643	N21–C24	π*	0.214	27.68	0.27	0.080
N29	n(1)	1.616	C25–C26	π*	0.335	37.24	0.29	0.094
N29	n(1)	1.616	C28–C34	π*	0.021	38.58	0.29	0.096

3.1.6 Molecular Electrostatic Potential (MEP) Analysis:

The molecular electrostatic potential (MEP) surface of ENIMHN was computed at the B3LYP/6-311G(d,p) level and mapped onto the 0.001 a.u. electron density isosurface over a potential range of -9.076×10^{-2} to $+9.076 \times 10^{-2}$ a.u. (**Fig. 7**), providing a color-coded visualization of charge distribution and reactive site identification across the molecular surface [38]. The most electron-rich region (deep red, V = -9.076×10^{-2} a.u.) is concentrated over the carbonyl oxygen O18 and hydroxyl oxygen O19 of the naphthohydrazide moiety, confirming these atoms as the primary nucleophilic and hydrogen-bond acceptor sites due to the high lone pair electron density localized on the oxygen atoms, consistent with their strong electron-donating character within the conjugated framework[39].

The most electron-deficient region (deep blue, V = $+9.076 \times 10^{-2}$ a.u.) is localized at the indole N–H hydrogen, identifying it as the principal electrophilic and hydrogen-bond donor site, while the peripheral aromatic C–H protons display cyan/light blue regions (V ≈ $+2 \times 10^{-2}$ to $+6 \times 10^{-2}$ a.u.), indicating moderately positive potential consistent with C–H···O and C–H···π type non-covalent interactions[40].

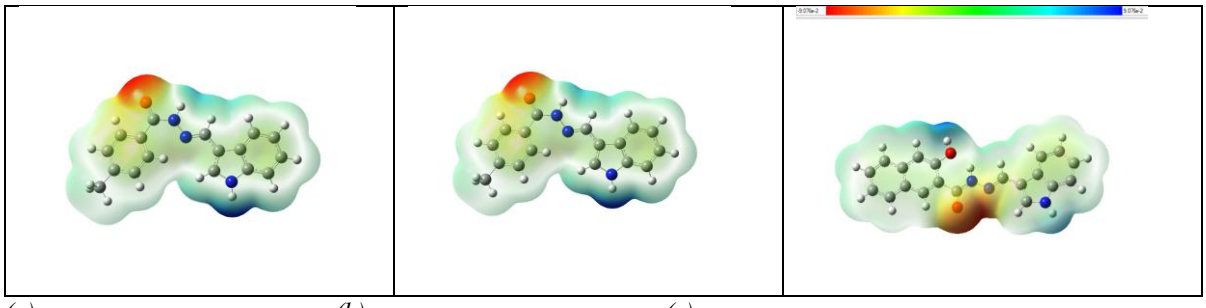

(a) *(b)* *(c)*

Figure 7. MEP surface of ENIMHN (a) view 1, (b) view 2, and (c) with scale bar; mapped at B3LYP/6-311G(d,p), range: -9.076×10^{-2} (red) to $+9.076 \times 10^{-2}$ a.u. (blue).

Intermediate yellow-orange potential regions are observed over the hydrazone nitrogen atoms N20 and N21, reflecting moderate nucleophilicity from the nitrogen lone pairs, while the naphthalene and indole aromatic ring carbons are covered by near-neutral green regions, confirming the extensive π-electron delocalization and the relatively uniform charge distribution across the fused aromatic

Journal of Molecular Science
Journal of Molecular Science
Volume 35 Issue 4, Year of Publication 2025, Page 1792-1805
DoI- 10.004687/1000-9035.2025.242

scaffold[41]. The pronounced spatial separation between the highly negative O18/O19 pole and the highly positive indole N–H pole, spanning the entire molecular backbone from the naphthohydrazide donor to the indole acceptor, is in direct agreement with the intramolecular charge transfer (ICT) direction established from FMO analysis and NBO analysis, collectively supporting the donor–acceptor push–pull electronic architecture and the potential nonlinear optical (NLO) activity of ENIMHN. The MEP analysis thus provides a complete reactivity map for ENIMHN: the oxygen-rich nucleophilic pole predicts preferential coordination to Lewis acid metal centers and interactions with electrophilic enzyme residues, the indole N–H electrophilic pole facilitates hydrogen bonding with protein carbonyl groups, and the aromatic π-surfaces support hydrophobic and π–π stacking interactions with aromatic amino acid residues, offering a quantum chemical rationale for the pharmacological activities reported for analogous hydrazone Schiff base compounds.

3.2 Molecular Docking Screening:

Here, three Sars-Covid-2 protease are taken, in which the **6LU7** is the crystal structure of the main protease (Mpro / 3CLpro) of SARS-CoV-2 complexed with an inhibitor. Mpro cleaves viral polyproteins into functional units essential for viral replication, making it a prime antiviral drug target. Second protease **6Y84** is another high-resolution structure of the same main protease (Mpro) but without a bound inhibitor (apo form). It is commonly used to study native active-site geometry and ligand accommodation. Third one, **6WCF** is the structure of the papain-like protease (PLpro) of SARS-CoV-2, which processes viral polyproteins and also interferes with the host immune response by deubiquitination and deISGylation activities.The three SARS-CoV-2 main protease targets (6wcf, 6y84, and 6lu7) exhibit distinct conformational states and active-site architectures, which directly explain the differential binding of ENIMHN. 6wcf represents an unliganded native state of the main protease (Mpro) with a fully accessible active-site cleft. **Table-7** revealed ENIMHN to achieve the highest binding affinity (−9.4 kcal/mol) via six stable hydrogen bonds (1.94–3.15 Å) to residues including PHE156, ASP157, and LEU126. In contrast, 6y84 is a peptide-bound form of Mpro where the active site is partially occupied, leading to reduced binding energy (−8.6 kcal/mol) and only four hydrogen bonds, notably with GLU14 and MET17 from the flexible N-terminal domain[42].

Table-7 Molecular docking parameters of ENIMHN with targeted protease

Ligand	Target Protein	Binding energy (kcal/mol)	Number of hydrogen bonds (distance in Å)	Protein bounded residues
ENIMHN	6wcf	-9.4	6 (2.53, 2.06, 1.94, 2.64, 2.75 & 3.15 Å)	PHE156, ASP157, LEU126, ALA139, VAL155, VAL49
	6y84	-8.6	4 (2.58, 2.79, 3.40 & 4.08Å)	GLU14, MET17, MET17, LYS97
	6lu7	-8.3	4 (2.81, 2.79, 3.03 & 3.66Å)	LEU141, SER144, HIS163, MET165

The another **6lu7** represents Mpro in complex with an inhibitor, causing significant conformational rearrangement of the catalytic dyad (HIS41-CYS145); thus ENIMHN showed the lowest affinity (−8.3 kcal/mol) with four hydrogen bonds to LEU141, SER144, HIS163 and MET165 residues adjacent to, but not directly at, the catalytic center. The decreasing binding energy trend (6wcf > 6y84 > 6lu7) inversely correlates with increasing active-site occlusion, validating that ENIMHN preferentially binds the unliganded, open conformation of SARS-CoV-2 Mpro. Remarkably, despite structural differences, the compound maintained four to six hydrogen bonds across all variants, with the best residue matching occurring in 6wcf (six distinct binding partners) versus the repeated MET17 interaction in 6y84, indicating a more promiscuous but less specific binding mode when the active site is obstructed[10]. These results suggest that ENIMHN is most effective against the native viral protease before substrate or inhibitor binding, highlighting its potential as a prophylactic rather than competitive-rescue inhibitor[42]. The 3D and 2D poses of docing are displayed in **Fig. 8**.

Journal of Molecular Science
Journal of Molecular Science
Volume 35 Issue 4, Year of Publication 2025, Page 1792-1805
DoI- 10.004687/1000-9035.2025.242

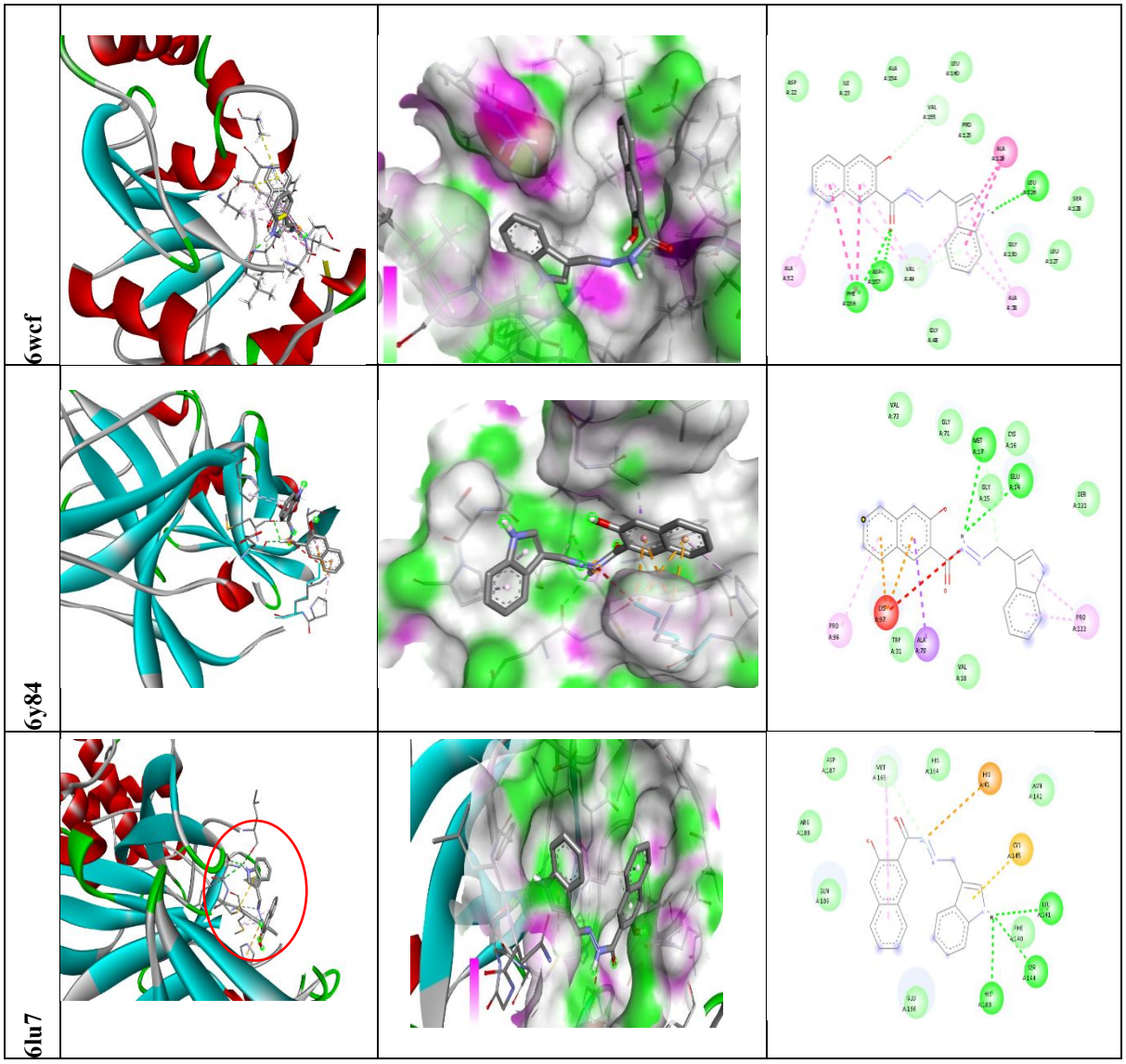

Figure-8 Molecular docking interactions of ENIMHN in 2D and 3D view

5. CONCLUSION:

The DFT/B3LYP/6-311G(d,p) optimization of ENIMHN confirmed a near-planar, extended π-conjugated geometry stabilized by an intramolecular O–H···O=C hydrogen bond, with computed bond parameters and vibrational frequencies showing excellent agreement with experimental FT-IR, Raman, and NMR data. Frontier molecular orbital analysis revealed a narrow HOMO–LUMO gap of 2.3179 eV with intramolecular charge transfer from the naphthohydrazide donor to the indole acceptor, while NBO analysis quantified key hyperconjugative interactions, most notably the n(1)(N20)→π*(C17–O18) stabilization energy of 64.59 kcal/mol, collectively confirming the strong electronic delocalization across the hydrazone scaffold. Molecular electrostatic potential mapping identified the carbonyl and hydroxyl oxygens as primary nucleophilic sites and the indole N–H as the principal electrophilic center, providing a quantum chemical rationale for the compound's reactivity and non-covalent interaction profile. Molecular docking against three SARS-CoV-2 protease targets yielded binding affinities of −9.4, −8.6, and −8.3 kcal/mol for 6WCF, 6Y84 and 6LU7 respectively, with up to six hydrogen bonds formed preferentially in the unliganded active-site conformation, establishing ENIMHN as a promising prophylactic-type antiviral scaffold.

ACKNOWLEDGEMENT:

The authors thank Department of Chemistry, Govt. Arts College, Chidambaram for providing research oppurtunities.

REFERENCES:

1. Rollas S, Küçükgüzel ŞG. Biological activities of hydrazone derivatives. *Molecules*. 2007;12:1910–1939. doi:10.3390/12081910.
2. Dhar DN, Sharma RL, Bansal GC. J Sci Ind Res. 1982;41:501–506.
3. Loncle C, Brunel JM, Vidal N, Dherbomez M, Letourneux

Y. Eur J Med Chem. 2004;39:1067–1071.
4. Masunari A, Tavares LC. Bioorg Med Chem. 2007;15:4229–4236.
5. Küçükgüzel SG, Rollas S, Küçükgüzel I, Kiraz M. Eur J Med Chem. 1999;34:1093–1100.
6. Imramovsky A, Polanc S, Vinsova J, Kocevar M, Jampilek J, Reckova Z, Kaustova J. Bioorg Med Chem. 2007;15:2551–2559.
7. Guantai EM, Ncokazi K, Egan TJ, Gut J, Rosenthal PJ, Smith PJ, Chibale K. Bioorg Med Chem. 2010;18:8243–8256.
8. Savini L, Chiasserini L, Travagli V, Pellerano C, Novellino E, Cosentino S, Pisano MB. Eur J Med Chem. 2004;39:113–122.
9. Vane JR, Botting RM. Inflamm Res. 1998;47:78–87.
10. Zhang L, Lin D, Sun X, Curth U, Drosten C, Sauerhering L, Becker S, Rox K, Hilgenfeld R. *Science*. 2020;368:409–412.
11. Becke AD. Density-functional thermochemistry. III. The role of exact exchange. J Chem Phys. 1993;98:5648–5652.
12. Frisch MJ, Trucks GW, Schlegel HB, et al. *Gaussian 09, Revision D.01*. Wallingford (CT): Gaussian Inc.; 2013.
13. Pires DEV, Blundell TL, Ascher DB. J Med Chem. 2015;58:4066–4072.
14. Abass M, Ismail M, Abdel-Monem W, Mayas A. Substituted pyridopyrimidinones. Part 5. Behavior of 2-hydroxy-4-oxo-4H-pyrido[1,2-α]pyrimidine-3-carbaldehyde in nucleophilic condensation reactions. Chem Pap. 2010;64:72–83. doi:10.2478/s11696-009-0100-0.
15. Lee C, Yang W, Parr RG. Phys Rev B. 1988;37:785–789.
16. Gilli G, Bellucci F, Ferretti V, Bertolasi V. J Am Chem Soc. 1989;111:1023–1028.
17. Foresman JB, Frisch Æ. *Exploring chemistry with electronic structure methods*. 3rd ed. Wallingford (CT): Gaussian Inc.; 2015.
18. Umar Y, Abdalla S. IOSR J Appl Chem. 2015;8(9):26–34.
19. Umar Y. IOSR J Appl Chem. 2015;8(7):44–55.
20. Çiğdem Y. Süleyman Demirel Univ J Sci. 2020;15(2):224–236.
21. Yuksektepe C, Saracoglu H, Caliskan N, Yilmaz I, Cukurovali A. J Korean Chem Soc. 2010;31(12):3553–3560.
22. Gümüş MK, Kaya Y, Koca M, Tüzün B, Kaya S. J Mol Struct. 2022;1268:133682.
23. Rozenberg M, Loewenschuss A, Marcus Y. Spectrochim Acta A. 2000;56:1587–1595.
24. Al-Abdullah ES, Al-Obaid AM, Al-Deeb OA, Habib EE, El-Emam AA. *Molecules*. 2022;27:4742.
25. Silverstein RM, Webster FX, Kiemle DJ. *Spectrometric identification of organic compounds*. 7th ed. Hoboken (NJ): John Wiley & Sons; 2005.
26. Almutairi MS, Alotaibi MR, Alotaibi NA, Alharbi AA. J Theor Comput Chem. 2019;18:1950008.
27. Çukurovalı A, Yılmaz I, Kılıç Z. J Mol Struct. 2010;979:105–112.
28. Clayden J, Greeves N, Warren S. *Organic chemistry*. 2nd ed. Oxford: Oxford University Press; 2012.
29. Pretsch E, Bühlmann P, Badertscher M. *Structure determination of organic compounds*. 4th ed. Berlin: Springer; 2009.
30. Berber I, Dasdag S, Genc M, Ates M, Kocer A. Arch Pharm. 1999;332:43–46.
31. Günther H. *NMR spectroscopy: basic principles, concepts, and applications in chemistry*. 3rd ed. Weinheim: Wiley-VCH; 2013.
32. Breitmaier E. *Structure elucidation by NMR in organic chemistry*. 3rd ed. Chichester: Wiley; 2002.
33. Wolinski K, Hinton JF, Pulay P. J Am Chem Soc. 1990;112:8251–8260.
34. Cheeseman JR, Trucks GW, Keith TA, Frisch MJ. J Chem Phys. 1996;104:5497–5509.
35. Fleming I. *Frontier orbitals and organic chemical reactions*. London: Wiley; 1976.
36. Shakdofa MME, Shtaiwi MH, Mortan N, Abdel-Rahem TM. Main Group Chem. 2014;13:187–218.
37. Weinhold F, Landis CR. *Valency and bonding: a natural bond orbital donor–acceptor perspective*. Cambridge: Cambridge University Press; 2005.
38. Murray JS, Sen K. *Molecular electrostatic potentials: concepts and applications*. Amsterdam: Elsevier; 1996.
39. Politzer P, Murray JS. Theor Chem Acc. 2002;108:134–142.
40. Desiraju GR, Steiner T. *The weak hydrogen bond in structural chemistry and biology*. Oxford: Oxford University Press; 1999.
41. Fukui K. *Science*. 1982;218:747–754.
42. Jin Z, Du X, Xu Y, Deng Y, Liu M, Zhao Y, Zhang B, Li X, Zhang L, Peng C, et al. *Nature*. 2020;582:289–293.